

Performance evaluation of the 8-inch MCP-PMT for Jinping Neutrino Experiment

Aiqiang Zhang^{a,b,c}, Benda Xu^{a,b,c,*}, Jun Weng^{a,b,c}, Huiyou Chen^{a,b,c}, Wenhui Shao^{a,b,c},
Tong Xu^{a,b,c}, Ling Ren^{a,b,c}, Sen Qian^d, Zhe Wang^{a,b,c}, Shaomin Chen^{a,b,c}

^aDepartment of Engineering Physics, Tsinghua University, Beijing, 100084, China

^bCenter for High Energy Physics, Tsinghua University, Beijing, 100084, China

^cKey Laboratory of Particle & Radiation Imaging (Tsinghua University), Ministry of Education, China

^dInstitute of High Energy Physics, Chinese Academy of Sciences, Beijing, 100049, China

Abstract

Jinping Neutrino Experiment plans to deploy a new type of 8-inch MCP-PMT with high photon detection efficiency for MeV-scale neutrino measurements. This work studies the performance of the MCP-PMTs, including the photon detection efficiency, the charge resolution of the single photoelectron, the transition time spread, single photoelectron response, rates of dark counts and after pulses. We find a long tail in the charge distribution, and combined with the high photon detection efficiency, the overall energy resolution sees substantial improvements. Those results will be provided as the inputs to detector simulation and design. Our results show that the new PMT satisfies all the requirements of the Jinping Neutrino Experiment.

Keywords: MCP-PMT, photon detection efficiency, Jinping Neutrino Experiment

PACS: 29.40.Mc

1. Introduction

The Jinping Neutrino Experiment (JNE) under construction is a hundred-ton liquid scintillator detector with Cherenkov and scintillation light readout at CJPL II [1, 2] with 2400 m rock overburden, targeting solar, terrestrial and supernovae neutrinos [3, 4, 5, 6]. Photomultiplier tubes (PMT) [7] are commonly used to detect individual photons in

*Corresponding author

Email address: orv@tsinghua.edu.cn (Benda Xu)

Preprint submitted to Elsevier

March 10, 2023

water Cherenkov [8, 9] and liquid scintillator detectors [10, 11]. It converts a photon into a photoelectron (PE) and then to a measurable electric signal. For the 8-inch form factor, instead of conventional dynodes, the micro-channel plate (MCP) PMT multiplies PEs inside the micro-channels, offering faster time response and high gain in a compact size [7, 12, 13].

Precise measurement of energy spectra demands affordable PMTs to achieve good photo-coverage with high photon detection efficiency (PDE¹). Cherenkov photons providing a directional measurement of solar neutrinos have 1.5 ns timing dispersion at a 10 m scale, setting the requirement of time precision to be ~ 1 ns.

The new type of 8-inch MCP-PMT (GDB-6082 [14]) is produced by North Night Vision Science & Technology (Nanjing) Research Institute Co. Ltd. (NNVT). Similarly structured 20-inch MCP-PMTs by NNVT were evaluated by the JUNO collaboration to have an average PDE of 28% [15]. Characterization of gain, single PE resolution, PDE, transit time spread (TTS) and dark count rate (DCR) is the key step to construct neutrino and dark matter detectors. Such tests have widely been carried out, for 8-inch dynode PMTs (9354KB, R5912, XP1806) at Daya Bay [16], 10-inch dynode PMTs (R7081) at Double Chooz [17], 8-inch dynode PMTs (CR365-02-1) at LHAASO [18], 20-inch dynode PMTs (R12860) and MCP-PMTs (GDB-6203) at HyperKamiokande [19], 3-inch dynode PMTs (R12199-02) at KM3NeT [20], 3-inch dynode PMTs (R11410-21) at XENON1T [21] and XENONnT [22], and 3-inch PMTs (R12199-01) at IceCube [23].

This work characterizes nine GDB-6082 MCP-PMT samples for the JNE. The setup of the testing facility is introduced in Section 2. The analysis methods and results of gain, charge resolution, PDE, TTS, DCR, shape of single electron response (SER), pre-pulse and after-pulse are described in Section 3. The boost for energy resolution is discussed in Section 4 with a summary in Section 5.

2. Experimental setup and procedures

The schematics of the PMT-test facility is shown in Fig. 1. CAEN V1751 1GS/s 10-bit digitizer is used to acquire data [24]. With the dynamic range of 1V, we use the

¹The product of PE collection and quantum efficiencies.

unit of “1 ADC” [25] to represent a quantization level of 1000/1024 mV in the following sections. Wiener EDS 30330p high voltage (HV) module [26] supplies a positive voltage for each PMT. A picosecond laser (PiL040XSM) from Advanced Laser Systems [27] produces 34 ps light pulses at 405 nm to illuminate the PMTs via an attenuator and feeds an electronic trigger signal into the digitizer. The digitizer, the HV module and the laser are controlled by self-developed data acquisition (DAQ) software² based on the CAENDigitizer [28], Net-SNMP [29] and PyVISA [30] libraries.

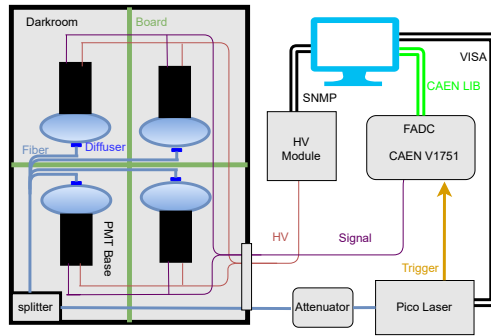


Figure 1: The schematics of the test system. The computer controls the HV module, laser, and FADC directly. The trigger signal from laser and waveforms from PMT are sampled by the FADC. The laser light is split into four channels and diffused after attenuation.

PMTs are installed in dark rooms made of a black light-tight plastic box separated by extruded polystyrene boards into four parts. A fiber splitter distributes attenuated laser light into the four dark rooms. Each channel ends with a 4 cm² diffuser plate to spread light onto the top of the PMT photocathode. A base distributes HV to the pins of each PMT and outputs the amplified pulse from the anode. A CR365 PMT [31] from Beijing Hamamatsu Photon Techniques Inc. is used as a reference for PDE measurements. It has a specification of 25 % quantum efficiency (QE) at 420 nm, and $0.97 \times 25 \%$ at 405 nm [7]. The PDE at 405 nm is estimated to be 17%, corresponding to a collection efficiency of 0.7–0.8 typical for 8-inch dynode PMTs [12, 32, 33].

The test procedures indicated in Fig. 2 are executed by DAQ software automatically. To lower the systematic errors from the light source variation and unknown splitter ratios, we permute the PMTs in the dark rooms to conduct PDE measurements and light source

²Github repo: <https://github.com/greatofdream/CAENReadout>.

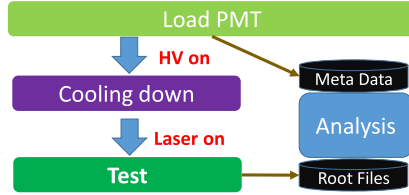


Figure 2: The flow chart of test procedures. PMTs are cooled down before DAQ. The procedures are executed automatically.

calibration simultaneously in Section 3.8. To cool down the DCR, all the PMTs stay in the darkroom with vendor-specified HV for at least 12 hours before the digitizer acquires waveforms with laser on. The waveforms are stored in ROOT [34] files and analyzed with self-developed software³.

3. Methods and results

3.1. Preanalysis

The laser intensity is adjusted to the level of 1/20 occupancy to obtain single PE events. The window size T_{wave} is 10 400 ns to include all the possible after-pulses (see Section 3.7). The rising edge of the trigger waveform from the laser system is linearly interpolated to get the half-height time t_{trig} at about 250 ns, as shown in Fig. 3.

In the preanalysis, we select a preliminary window $[t_{\text{trig}}, 600 \text{ ns}]$ where dark noises ($<10 \text{ kHz}$ in Section 3.6) and laser pulses are expected to contribute 0.004 and 0.05 counts on average. The peak time t_p is the minimum position in each window, as shown in Fig. 3.

The nonzero baseline is estimated from the sidebands $[-200 \text{ ns}, -10 \text{ ns}]$ and $[100 \text{ ns}, 200 \text{ ns}]$ relative to t_p . To remove potential additional pulses in the sidebands, we define a voltage threshold from a rough estimation of white noise as the horizontal violet dotted line in Fig. 3 and cut off additional 10 ns around each over-threshold time interval. The baseline μ_b is estimated as the average of the residual sidebands. The peak height V_p of a pulse is the difference between μ_b and the minimum voltage at t_p .

³Github repo: <https://github.com/greatofdream/pmtTest>.

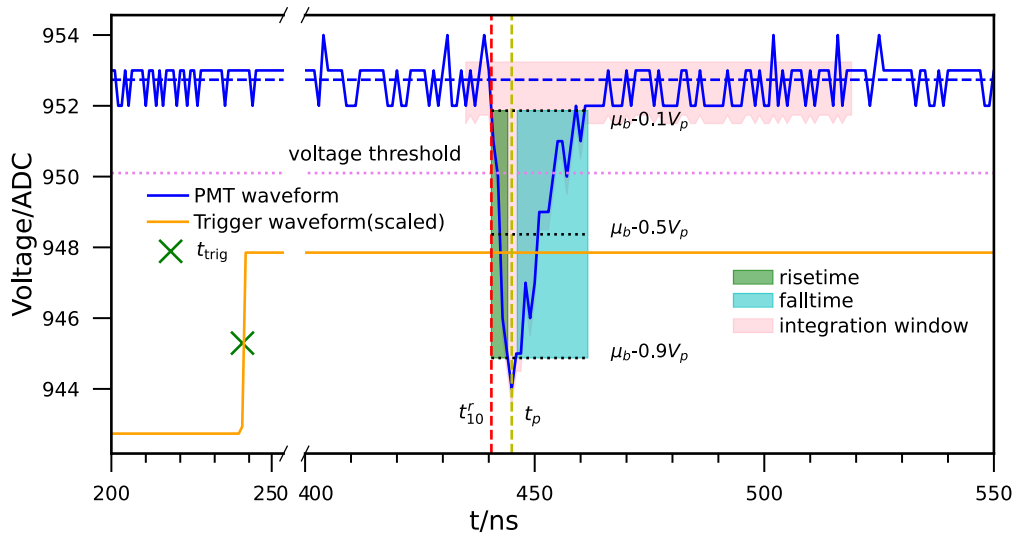


Figure 3: An example of PMT and trigger signals. The orange line is the trigger waveform in arbitrary scale. The green cross is the interpolated trigger time t_{trig} . The solid blue line is the PMT waveform with a PE pulse. The horizontal violet dotted line is the voltage threshold for calculating the baseline shown by the blue horizontal dashed line. The black horizontal dash lines intersect 10%, 50% and 90% of (downward) rising and falling edges. The rise and fall times are the interval lengths between 10% and 90% of the respective edges. The red and yellow vertical dashed lines are for the 10% rising edge and the pulse peak.

Over all the waveform samples, a Gaussian $f(t; t_0, \sigma_{t_0}^2)$ is fitted to the distribution of $t_p - t_{\text{trig}}$ of pulses whose V_p exceeds 5 ADC. We define a new candidate window, about 30 ns long, as $[t_0 - 5\sigma_{t_0}, t_0 + 5\sigma_{t_0}]$ to calculate new t_p and V_p by repeating the above procedures. The contracted time window reduces the dark counts by 10 times, with which we shall conduct the charge and time characterization of the single PE in the following sections.

3.2. Single-PE charge spectrum and resolution

Considering the rise and fall time distributions, the charge Q of a pulse is defined as the summation of the baseline-subtracted voltages in a time window $[-10 \text{ ns}, 75 \text{ ns}]$ relative to t_p as illustrated in the pink region of Fig. 3. The input impedance being 50Ω [24], the charge in Coulomb is $Q/50 \Omega$.

Such Q in Fig. 4a represents the charge of a single PE with negligible multi-PE contributions due to the low occupancy. A long tail is evident in the single-PE charge distribution, which was also found in the NNVT 20-inch MCP-PMTs by the JUNO collaboration [15]. Zhang et al. [35] proposed a phenomenological parameterization without dedicated consideration of the multiplication process of the PEs. We shall discuss the physical model and solution of the long tail in our future publications.

To describe the peak shape of the Q distribution, a Gaussian function $N^{1e}f(Q; Q_0, \sigma_{Q_0}^2)$ is fitted to the interval $[0.65Q_0, 1.35Q_0]$ via the modified least-square (MLS) [36] illustrated as the red line in Fig. 4a. To remove the influence of the pedestal and describe the long tail, N^{hit} pulses with $V_p > 3 \text{ ADC}$ and $Q > 0.25Q_0$ are selected to calculate the mean \bar{Q} and sample variance s_Q^2 of Q . The Gaussian component ratio N^{1e}/N^{hit} (0.59 ± 0.02 for the nine MCP-PMTs) of charge distribution reflects the significance of long tail.

The gains of the main peak and the entire sample are $Q_0/(50 \Omega e) \approx 10^7$ and $\bar{Q}/(50 \Omega e)$, e being the charge of an electron. The relative *peak* and *sample resolutions* ν_0 and ν are defined as σ_{Q_0}/Q_0 and $\sqrt{s_Q^2}/\bar{Q}$. Fig. 4b indicates that \bar{Q} is about 1.8 times Q_0 for the MCP-PMTs, in agreement with Zhang et al. [35]. The long tail causes the resolution of MCP-PMTs to degrade from $\nu_0 = 0.25 \pm 0.02$ to $\nu = 0.69 \pm 0.03$, which is less pronounced for the reference dynode PMT.

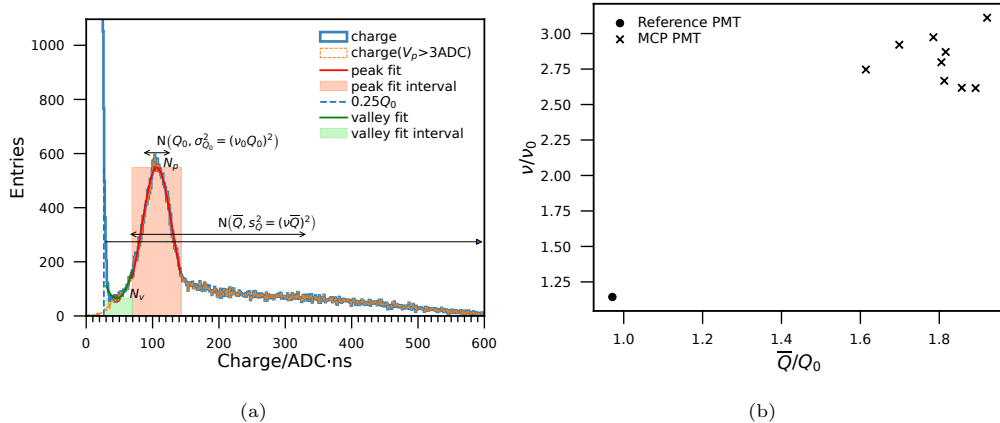


Figure 4: (a) The long-tailed single-PE charge distribution of an MCP-PMT. The entries around zero are waveforms with no signal. The vertical blue dashed line is the pedestal cut. The orange histogram is the selected waveforms with peak-height cut ($V_p > 3\text{ADC}$). The pink and green areas are the fit intervals for the peak and valley parameters. A Gaussian function $f(Q; Q_0, \sigma_{Q_0}^2)$ is fitted to the peak of single-PE charge distribution. Mean \bar{Q} and sample variance s_Q^2 of selected charge reflect the long-tailed information. (b) The charge and resolution ratios show the effect of the long tail. The point and crosses represent the reference and MCP-PMTs, respectively.

3.3. Peak-to-valley ratio

A parabolic function is fitted to the valley based on MLS in the interval $[-0.15Q_0, 0.25Q_0]$ relative to the least-counted bin of the histogram between the pedestal and the main peak, as shown in Fig. 4a. The *valley count* N_v is defined as the minimum of the parabola and *peak count* N_p is the maximum of the Gaussian described in Section 3.2. The peak-to-valley ratio (P/V) N_p/N_v shows the ability to discriminate between electronic noises and a PE signal. The average P/V of MCP-PMTs is about 5.9, significantly higher than that (about 2.4) of the reference PMT.

3.4. Single electron response

We define $t_r^{10}, t_r^{50}, t_r^{90}$ ($t_f^{10}, t_f^{50}, t_f^{90}$) as the times of interpolated 10%, 50%, and 90% V_p in the rising (falling) edge as shown in Fig. 3. The rise time $t_r = t_r^{90} - t_r^{10}$, fall time $t_f = t_f^{10} - t_f^{90}$ and full width at half maximum $\text{FWHM} = t_f^{50} - t_r^{50}$ describe the shape of *single electron response* (SER). They are measured to be $t_r = 3.72 \pm 0.15$ ns, $t_f = 15.6 \pm 1.8$ ns and $\text{FWHM} = 9.07 \pm 0.63$ ns for the nine MCP-PMTs.

To get a smooth SER, signals with $V_p > 3 \text{ ADC}$, $Q \in [0.5Q_0, 1000 \text{ ADC} \cdot \text{ns}]$ and $\text{FWHM} \in [2 \text{ ns}, 15 \text{ ns}]$ are selected to exclude the noise and large pulses. An *exGaussian* distribution $f^N(t; \mu_{\text{SER}}, \sigma_{\text{SER}}^2) \otimes f^{\text{Exp}}(t; 1/\tau_{\text{SER}})$ [37] is used to fit the SER, in which μ_{SER} is the pulse location, σ_{SER} and τ_{SER} model its shape. They are measured to be $\tau_{\text{SER}} = 7.2 \pm 1.1 \text{ ns}$ and $\sigma_{\text{SER}} = 1.62 \pm 0.06 \text{ ns}$ for the nine MCP-PMTs.

3.5. Transit time spread

As shown in Fig. 5, the PEs from the photocathode drift to the MCP. Using a model of a cathode at 0 V, a focusing electrode at 480 V and an MCP at 528 V to simulate the electric field and the PE trajectory, we find the PEs from the top of the photocathode with 0 eV and 3 eV kinetic energies have drift times of about 21 ns and 18 ns respectively. A PE entering an MCP channel is multiplied to be an observable pulse, while that hitting the surface of the MCP gets scattered inelastically into several secondary electrons or elastically into one single electron [38]. The scattered electrons drift in the electric field until finally entering the MCP channels to give delayed pulses [20]. Multiple secondary electrons with different kinetic energies may cause two or more pulses with different drift times, one example shown in Fig. 6a.

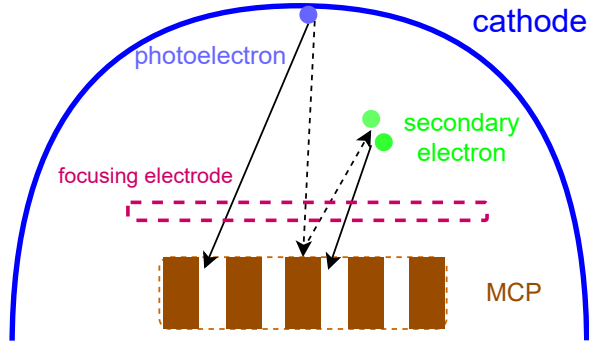


Figure 5: The PEs drift from the photocathode to the MCP and get amplified or scattered.

The time of a PE traveling from the photocathode to the anode is called the *transit time* (TT). However, the absolute TT is hard to measure. As a convention practically, we refer to the time difference between the trigger signal t_{trig} and 10% of the rise time of a PE pulse t_r^{10} as TT instead. The TT distribution of the MCP-PMTs contains slowly

rising and falling edges on both sides of the peak, as shown in Fig. 7a. The rising edge is due to the PEs with larger kinetic energies, while the falling one consists of secondary electrons with longer drift times [39].

Delayed pulses are searched in the interval $[t_0 + 20 \text{ ns}, t_0 + 80 \text{ ns}]$ to separate them from the main pulses in $[t_0 - 5 \text{ ns}, t_0 + 5 \text{ ns}]$. The blue histogram in Fig. 6b is the distribution of the delayed pulses, and the filled one is for those with the main pulses in the same waveform, an example demonstrated in Fig. 6a. The sharp difference between them at about 40 ns after the main peak, twice the drift time of PEs from the cathode to the MCP, reasonably illustrates that an elastically scattered electron cannot appear together with a main pulse in a waveform.

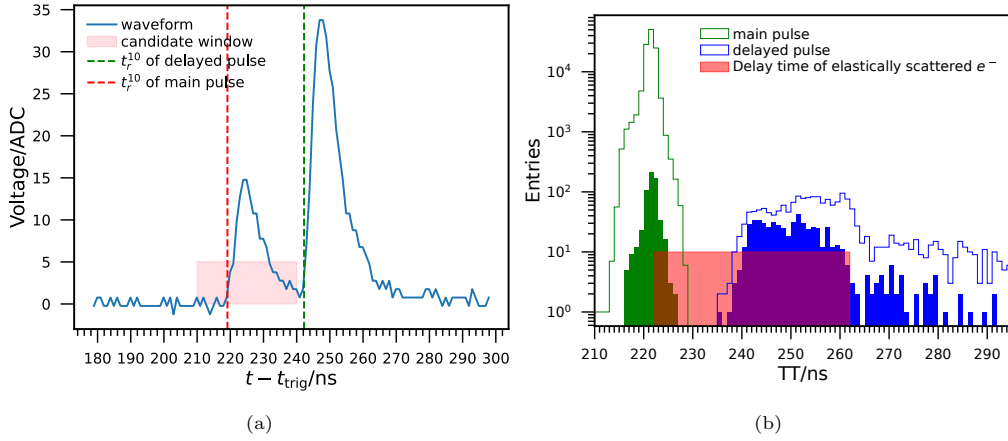


Figure 6: (a) Double-pulse example. The first pulse falls in the candidate window defined in Section 3.1. (b) The green and blue histograms are the main and delayed pulse distributions, respectively. The filled histograms are waveforms containing the main and delayed pulses simultaneously.

In Fig. 7a, the main and early components are modeled with Gaussian functions $N_1 f_1^N(t; \mu_{TT}, \sigma_{TT}^2)$ and $N_2 f_2^N(t; \mu_K, \sigma_K^2)$, with the subscript K standing for high-kinetic-energy PEs. Considering the exponential distribution of kinetic energies of secondary electrons [38, 40], $f^{\text{Exp}}(t; 1/\tau_S)$ is suitable to model the delayed component. We add a constant b_S and a translation of $\mu_{TT} + 3\sigma_{TT}$ to fit the data. The 0.5 ns-binned TT

histogram with selection criteria in Section 3.2 is fitted by

$$\begin{aligned}
& B + N_1 f_1^N(t; \mu_{\text{TT}}, \sigma_{\text{TT}}^2) \\
& + N_2 f_2^N(t; \mu_K, \sigma_K^2) \\
& + b_S H(\mu_{\text{TT}} + 3\sigma_{\text{TT}}) + N_S f^{\text{Exp}}\left(t - (\mu_{\text{TT}} + 3\sigma_{\text{TT}}); \frac{1}{\tau_S}\right)
\end{aligned} \tag{1}$$

in which H is the Heaviside function to restrict the domain of the delayed component, and B is the constant dark noise rate. The early and exponential components are as small as $N_2/N_1 = 0.026 \pm 0.018$, $N_S/N_1 = 0.010 \pm 0.003$ and $2b_S\sigma_{\text{TT}}/N_1 = 0.00026 \pm 0.00009$ for the nine MCP-PMTs. σ_K , τ_S and $\mu_{\text{TT}} - \mu_K$ are fitted to be 1.4 ± 0.3 ns, 1.1 ± 0.1 ns and 3.0 ± 0.4 ns. TTS (1.73 ± 0.08 ns) is defined as $\text{FWHM} = 2\sqrt{2 \ln 2} \sigma_{\text{TT}}$ [7] representing the timing resolution. The charge and TT seem to be correlated in Fig. 7b and the long tail is evident in charge distribution.

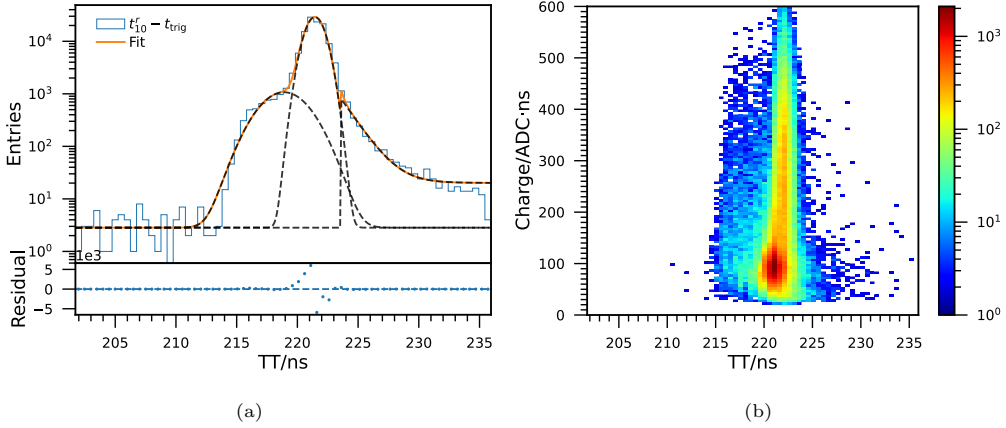


Figure 7: (a) The top pad is the distribution of TT with the y-axis in the logarithmic scale. The black dashed lines from left to right are early, main and delayed components with a dark noise pedestal. The bottom pad is the residual between data and fit in linear scale. (b) The 2D distribution of TT and charge with the colorbar in logarithmic scale.

3.6. Dark count rate and pre-pulse

The dark noise mimicking PEs mainly comes from the spontaneous thermionic electrons emitted from the photocathode [20]. The dark count rate (DCR) is $N^{\text{noise}}/(N^t T_{\text{DCR}})$, in which N^t is the number of total waveforms and N^{noise} is the noise count in the

interval of $[-300\text{ ns}, -150\text{ ns}]$ relative to the peak time μ_{TT} of TT distribution with $T_{\text{DCR}} = 150\text{ ns}$. The DCR of nine MCP-PMTs is $5.8 \pm 1.6\text{ kHz}$ at room temperature.

Generated from photons hitting the MCP or the first dynode directly rather than the photocathode, *pre-pulses* appear about tens of nanoseconds earlier with smaller amplitudes [15]. The probability P_{pre} of pre-pulses is $N^{\text{pre}}/N^{\text{t}} - \text{DCR} \cdot T_{\text{pre}}$, in which N^{pre} is the pre-pulse count of the total waveforms in the interval $[-100\text{ ns}, -10\text{ ns}]$ ($T_{\text{pre}} = 90\text{ ns}$) relative to μ_{TT} . The small P_{pre} ($1 \times 10^{-6} \pm 6 \times 10^{-6}$) is dominated by DCR at our low-occupancy setup.

3.7. After-pulse

Ions such as H^+ , He^+ and O^+ produced from gaseous impurities in the vacuum bulb by the PEs drift back to the photocathode, generate new electrons and then *after-pulses* [15, 41]. The delay times of after-pulses are proportional to the square root of the mass-to-charge ratios of the ions [21, 41, 42]. The after-pulses are searched from 200 ns

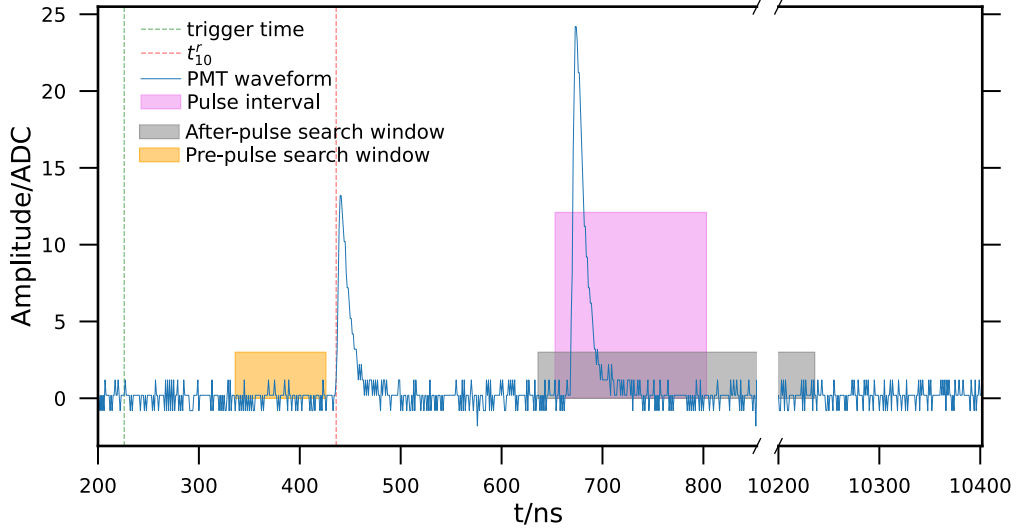


Figure 8: An example waveform for searching pre-pulses and after-pulses. Green and red vertical dashed lines are the trigger time and 10% of the rising edge of the main pulse t_r^{10} , respectively. The gray and orange regions are the intervals for searching after-pulses and pre-pulses.

after the main pulse in N^{hit} selected waveforms mentioned in Section 3.2. The 10% rise

Table 1: After-pulse parameters of MCP-PMTs

	H ⁺	H ₂ ⁺	He ⁺	CH ₄ ⁺	N ₂ ⁺ or O ₂ ⁺
t_i/ns	300±4	414±25	596±53	1180±28	1714±29
$A_i/N^{\text{hit}}/10^{-3}$	1.6±1.1	0.5±0.3	0.2±0.2	1.1±0.7	1.9±0.6
σ_i/ns	16±6	46±9	33±10	44±11	70±20
Q_i/Q_0	34±4	-*	22±3	18±3	14±2
σ_{Q_i}/Q_0	12±2	-*	17±3	9±1	8±1

* The charge of the 2nd structure cannot be fitted due to the interference with H⁺.

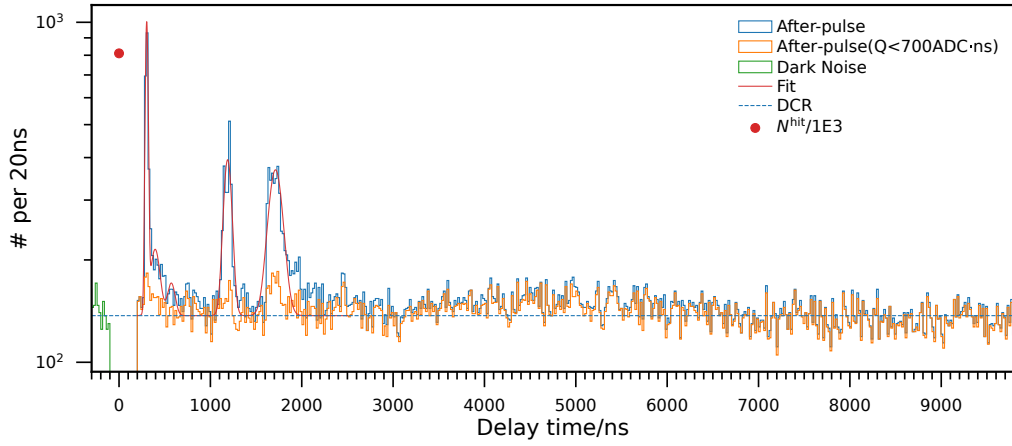
time t_r^{10} and charge Q of the after-pulse and pre-pulse are calculated in the $[-10 \text{ ns}, 75 \text{ ns}]$ window relative to the peak position, as shown by the violet area in Fig. 8.

The probability P_{after} of after-pulses is $N^{\text{after}}/N^{\text{hit}} - \text{DCR} \cdot T_{\text{after}}$, in which N^{after} is the pulse counts in $[200 \text{ ns}, 9800 \text{ ns}]$ ($T_{\text{after}} = 9600 \text{ ns}$) relative to the main pulses. P_{after} of nine MCP-PMTs is 0.009 ± 0.005 .

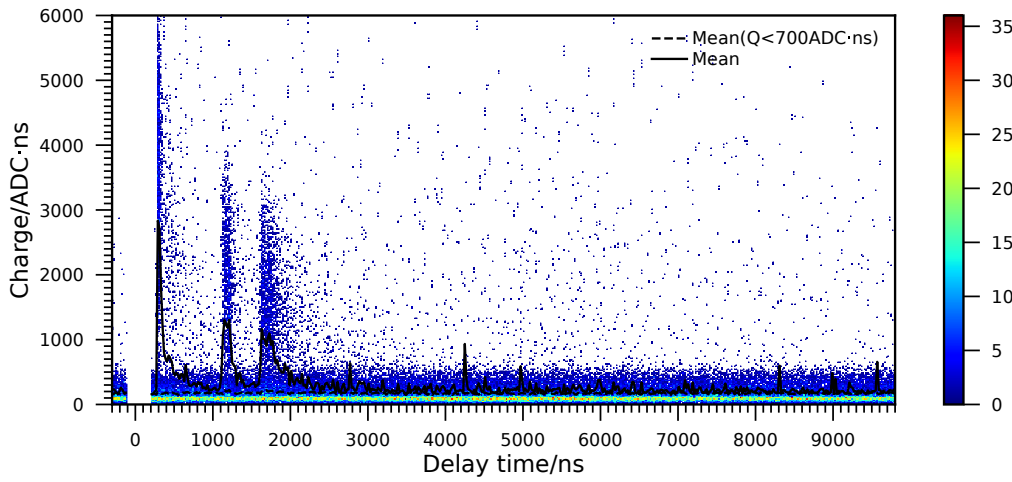
The distribution of the delay time from t_r^{10} of the main to after-pulse in Fig. 9a indicates five structures at around 300 ns, 400 ns, 600 ns, 1200 ns and 1700 ns, time ratio being about $1 : \sqrt{2} : \sqrt{4} : \sqrt{16} : \sqrt{32}$. These structures may originate from H⁺, H₂⁺, He⁺, CH₄⁺, and N₂⁺ or O₂⁺. XENON1T [21] and XMASS [43] gave the same assumptions for the first peak. But similar works by JUNO [44] and KM3NeT [20] assigned the first peak to H₂⁺.

We use five Gaussians with DCR ($\sum_{i=1}^5 A_i f_i^{\text{AP}}(t; t_i, \sigma_i^2) + \text{DCR} \cdot N^{\text{hit}}$) to model the five structures, in which A_i , t_i , and σ_i are the amplitudes, times, width of each after-pulse structure (Table. 1). A slow undulating structure contributes about half of the after-pulses on average in $[2000 \text{ ns}, 7000 \text{ ns}]$ as shown in Fig. 9a, whose origin we are unable to identify.

The after-pulses contain large charge signals, as shown in Fig. 9b. The charge distributions in $[t_i - 3\sigma_i, t_i + 3\sigma_i]$ of each after-pulse are scaled to the same dark noise count in Fig. 10. Charge distribution of the second structure (H₂⁺) is hard to fit due to the interference with the first one (H⁺). We fit each charge distribution with a Gaussian $f_i^{\text{APQ}}(Q; Q_i, \sigma_{Q_i}^2)$, in which Q_i and σ_{Q_i} are the charge and spread of each after-pulse (Table. 1). Because the 3rd-structure charge distribution is dominated by charge less



(a)



(b)

Figure 9: (a) An example of time distributions of dark noises (green), after-pulses (blue) and after-pulses with charge cut (orange) for an MCP-PMT, where the red line shows the Gaussian fits. The red point represents N^{hit} at 0 ns, around which the pre-pulses and delayed pulses are not shown. The horizontal dash line illustrates the expected dark-noise level. (b) Charge versus time distribution of pre-pulses and after-pulses. The bright horizontal band at about 100 ADC · ns mainly contains dark noise. The black (dash) line is the mean charge of (selected) pulses in each time bin.

than 700 ADC·ns as shown in Fig. 9b and Fig. 10, σ_{Q_3} from fitting on low-statistic entries contains large uncertainty and maybe unreliable. From the six PMTs with higher occupancies, the mean charge of each after-pulse shows a negative correlation between charge and delay time.

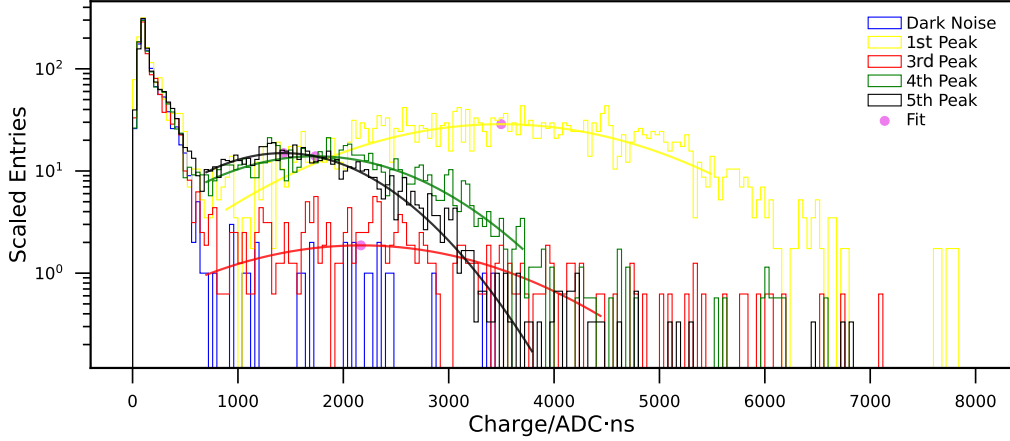


Figure 10: The charge distribution of after-pulse structures of an example MCP-PMT. The blue histogram is the distribution of dark noise. The violet points are the peaks of fit curves.

3.8. Relative photon detection efficiency

A regression method is developed to combine the light-source calibration and PDE measurements simultaneously. Let I_n denote the light intensity of the n th run, α_j the light allocation ratio of the j th splitter channel (out of four and assumed to be stable across runs), and ϵ_k the PDE of the k th PMT (out of one reference dynode and nine MCP-PMTs). The PE counts in each waveform follow Poisson distribution $\pi(I_n \alpha_j \epsilon_k)$.

For convenience, the index of the reference PMT is set to 0. Let $\alpha_j^0 \equiv \alpha_j / \alpha_0$, $\epsilon_k^0 \equiv \epsilon_k / \epsilon_0$, $I_n^0 \equiv I_n \alpha_0 \epsilon_0$. The hit rate $R_{nj k}$ of the k th PMT at the j th channel in the n th run is

$$R_{nj k} = 1 - \exp(-I_n \alpha_j \epsilon_k) = 1 - \exp\left(-e^{\log I_n^0 + \log \alpha_j^0 + \log \epsilon_k^0}\right). \quad (2)$$

The number of hit waveforms $N_{nj k}^{\text{hit}}$ of the k th PMT in the n th run with the j th channel follows Binomial distribution $B(N_{nj k}^{\text{hit}}; R_{nj k}, N_{nj k}^t)$, in which $N_{nj k}^t$ is the total

number of waveforms by the laser trigger. The likelihood is therefore

$$\mathcal{L} = \prod_{njk} R_{njk}^{N_{njk}^{\text{hit}}} (1 - R_{njk})^{N_{njk}^t - N_{njk}^{\text{hit}}}. \quad (3)$$

Eqs. (2) and (3) define a *Binomial regression* with *complementary log-log* link function [45], with $\log \epsilon_k^0$, $\log \alpha_j^0$ and $\log I_n^0$ as parameters. The relative PDEs ϵ_k^0 of MCP-PMTs are calculated from the regression results to be about 1.71, significantly higher than the reference PMT. We could attribute it to the improvements on both quantum and collection efficiencies of the GDB-6082 MCP-PMTs.

4. Energy resolution boost

Assume the PE counts N on a PMT with PDE ϵ for an event with visible energy E obeys Poisson distribution $\pi(\lambda_N = K\epsilon E)$, where K is a factor related to light yield and detector optics. The output total charge $\sum Q$ is a compound Poisson random variable with the expectation $E[\sum Q] = \lambda_N E[Q]$ and variance $\text{Var}[\sum Q] = E^2[Q]\lambda_N + \lambda_N \text{Var}[Q]$. The energy is estimated as $\hat{E} = \sum Q / (K\epsilon E[Q])$ with its resolution being

$$\frac{\sqrt{\text{Var}[\hat{E}]}}{E[\hat{E}]} = \frac{\sqrt{E^2[Q]\lambda_N + \lambda_N \text{Var}[Q]}}{\lambda_N E[Q]} = \frac{\sqrt{1 + \frac{\text{Var}[Q]}{E^2[Q]}}}{\sqrt{K\epsilon E}}. \quad (4)$$

The PMT specific factors are ϵ (proportional to relative PDE ϵ^0) and $1 + \text{Var}[Q]/E^2[Q]$ (estimated by the sample resolution ν^2 in Section 3.2). The latter is known as the *excess noise factor* [15, 46, 47] indicating the impact of single-PE charge smearing on energy. We plot the *figure of merit* $M_E \equiv \sqrt{(1 + \nu^2)/\epsilon^0}$ of the reference and nine MCP-PMTs in Fig. 11. Despite the long tail in the charge distribution, the boost of PDE of MCP-PMTs leads to a 10% better M_E . Because of that, considering the long tail to be an undesired by-product of MCP coating to improve the collection efficiency, we decide to adopt the technology. We are developing an advanced waveform analysis method to model the charge distribution and count PEs that may eliminate the long-tail degradation on energy resolution.

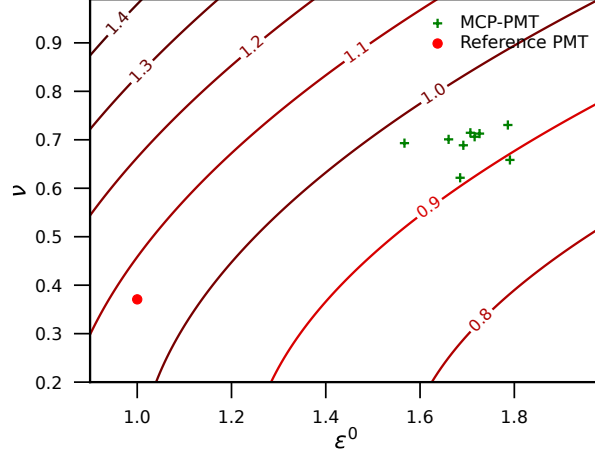


Figure 11: Contour map of energy resolution figure-of-merit M_E (see text) as a function of the sample resolution ν and the relative PDE ϵ^0 . The relative PDE of the reference PMT is 1.

Table 2: Summary of important parameters of the MCP-PMTs

Parameters	Value	Criteria	Notes	Section
\bar{Q}/Q_0	1.8 ± 0.1		Entire-Sample to Main-Peak Gain Ratio	3.2
$\nu_0 = \sigma_{Q_0}/Q_0$	0.25 ± 0.02		Peak Resolution	3.2
$\nu = \sqrt{s_Q^2}/\bar{Q}$	0.69 ± 0.03		Sample Resolution	3.2
N^{1e}/N^{hit}	0.59 ± 0.02		Main-peak Fraction	3.2
P/V	5.9 ± 1.4	> 5	Peak-to-Valley Ratio	3.3
t_r/ns	3.71 ± 0.15	< 4	Rise Time	3.4
t_f/ns	15.6 ± 1.8	< 20	Fall Time	3.4
$\sigma_{\text{SER}}/\text{ns}$	1.63 ± 0.06		Shape Parameters of SER	3.4
$\tau_{\text{SER}}/\text{ns}$	7.2 ± 1.1			
TTS/ns	1.73 ± 0.08	< 1.8	Transit Time Spread	3.5
DCR/kHz	5.8 ± 1.6	~ 5	Dark Count Rate	3.6
P_{pre}	$1\text{E-}6 \pm 6\text{E-}6$	< 0.001	Pre-Pulse Probability	3.7
P_{after}	0.009 ± 0.005	< 0.048	After-Pulse Probability	3.7
ϵ^0	1.71 ± 0.06	> 1.6	Relative PDE	3.8

5. Summary

The characteristics of the nine MCP-PMTs discussed are summarized in Table 2, which can be served as inputs to detector simulation and data analysis. A new calibration method based on regression in this study gives the average relative PDE of the MCP-PMT to be about 1.7 times the reference PMT. The long tail in the charge distribution is countered by the high PDE, resulting in an overall boost in energy resolution. We conclude that the new 8-inch GDB-6082 MCP-PMT from NNVT is suitable for the upcoming JNE.

6. Acknowledgments

This work is supported in part by the National Natural Science Foundation of China (12127808), the Key Laboratory of Particle & Radiation Imaging (Tsinghua University).

References

- [1] J. Li, X. Ji, W. Haxton, J. S. Y. Wang, The Second-phase Development of the China JinPing Underground Laboratory, *Physics Procedia* 61 (2015) 576–585. URL: <https://www.sciencedirect.com/science/article/pii/S1875389214006683>. doi:10.1016/j.phpro.2014.12.055.
- [2] J.-P. Cheng, K.-J. Kang, J.-M. Li, J. Li, Y.-J. Li, Q. Yue, Z. Zeng, Y.-H. Chen, S.-Y. Wu, X.-D. Ji, H. T. Wong, The China Jinping Underground Laboratory and Its Early Science, *Annual Review of Nuclear and Particle Science* 67 (2017) 231–251. URL: <https://doi.org/10.1146/annurev-nucl-102115-044842>. doi:10.1146/annurev-nucl-102115-044842.
- [3] J. F. Beacom, S. Chen, et al., Physics prospects of the Jinping neutrino experiment, *Chinese Physics C* 41 (2017) 023002. URL: <https://doi.org/10.1088/1674-1137/41/2/023002>. doi:10.1088/1674-1137/41/2/023002.
- [4] B. Xu, Jinping Neutrino Experiment: a Status Report, *J. Phys.: Conf. Ser.* 1468 (2020) 012212. URL: <https://dx.doi.org/10.1088/1742-6596/1468/1/012212>. doi:10.1088/1742-6596/1468/1/012212.
- [5] B. Xu, Innovations of the Upcoming Hundred-Ton Jinping Neutrino Experiment, 2022. URL: <https://zenodo.org/record/6816491>. doi:10.5281/zenodo.6816491.
- [6] B. Xu, Design and Construction of hundred-ton liquid neutrino detector at CJPL II, in: *Proceedings of 41st International Conference on High Energy physics — PoS(ICHEP2022)*, volume 414, SISSA Medialab, 2022, p. 926. URL: <https://pos.sissa.it/414/926>. doi:10.22323/1.414.0926.

- [7] Hamamatsu Photonics K.K., PHOTOMULTIPLIER TUBES: Basics and Applications FOURTH EDITION, available at https://www.hamamatsu.com/content/dam/hamamatsu-photonics/sites/documents/99_SALES_LIBRARY/etd/PMT_handbook_v4E.pdf (accessed on December 31, 2022), 2017.
- [8] A. Bellerive, et al., The Sudbury Neutrino Observatory, *Nuclear Physics B* 908 (2016) 30–51. doi:<https://doi.org/10.1016/j.nuclphysb.2016.04.035>, neutrino Oscillations: Celebrating the Nobel Prize in Physics 2015.
- [9] S. Fukuda, et al., The Super-Kamiokande detector, *Nuclear Instruments and Methods in Physics Research Section A* 501 (2003) 418–462. doi:[https://doi.org/10.1016/S0168-9002\(03\)00425-X](https://doi.org/10.1016/S0168-9002(03)00425-X).
- [10] A. Gando, et al. (The KamLAND Collaboration), Constraints on θ_{13} from a three-flavor oscillation analysis of reactor antineutrinos at KamLAND, *Phys. Rev. D* 83 (2011) 052002. URL: <https://link.aps.org/doi/10.1103/PhysRevD.83.052002>. doi:10.1103/PhysRevD.83.052002.
- [11] F. An, et al. (JUNO), Neutrino Physics with JUNO, *J. Phys. G* 43 (2016) 030401. doi:10.1088/0954-3899/43/3/030401. arXiv:1507.05613.
- [12] Y. Wang, et al., A new design of large area MCP-PMT for the next generation neutrino experiment, *Nuclear Instruments and Methods in Physics Research Section A: Accelerators, Spectrometers, Detectors and Associated Equipment* 695 (2012) 113–117. URL: <https://www.sciencedirect.com/science/article/pii/S0168900211023199>. doi:<https://doi.org/10.1016/j.nima.2011.12.085>, new Developments in Photodetection NDIP11.
- [13] Q. Wu, et al. (MCP-PMT workgroup), Summary of the R&D of 20-inch MCP-PMTs for neutrino detection, *JINST* 16 (2021) C11003. doi:10.1088/1748-0221/16/11/C11003.
- [14] Northern Night Vision Technology Ltd, Large Area MCP-PMT, available at <http://www.yskjinj.com/product/common/assets/upload/2022/0302/113755f9.pdf> (accessed on December 31, 2022), 2022.
- [15] A. Abusleme, et al. (JUNO), Mass testing and characterization of 20-inch PMTs for JUNO, *Eur. Phys. J. C* 82 (2022) 1168. doi:10.1140/epjc/s10052-022-11002-8. arXiv:2205.08629.
- [16] D. Liu, PMT evaluation for the Daya Bay neutrino experiment, in: 2008 IEEE Nuclear Science Symposium Conference Record, 2008, pp. 3133–3139. doi:10.1109/NSSMIC.2008.4775017.
- [17] E. Calvo, M. Cerrada, C. Fernandez-Bedoya, I. Gil-Botella, C. Palomares, I. Rodriguez, F. Toral, A. Verdugo, Characterization of large area photomultipliers under low magnetic fields: Design and performances of the magnetic shielding for the Double Chooz neutrino experiment, *Nucl. Instrum. Meth. A* 621 (2010) 222–230. doi:10.1016/j.nima.2010.06.009. arXiv:0905.3246.
- [18] K. Jiang, et al., Qualification tests of 997 8-inch photomultiplier tubes for the water Cherenkov detector array of the LHAASO experiment, *Nucl. Instrum. Meth. A* 995 (2021) 165108. doi:10.1016/j.nima.2021.165108. arXiv:2009.12742.
- [19] C. Bronner, Y. Nishimura, J. Xia, T. Tashiro, Development and performance of the 20" PMT for Hyper-Kamiokande, *Journal of Physics: Conference Series* 1468 (2020) 012237. URL: <https://doi.org/10.1088/1742-6596/1468/1/012237>. doi:10.1088/1742-6596/1468/1/012237.
- [20] S. Aiello, et al. (KM3NeT), Characterisation of the Hamamatsu photomultipliers for the KM3NeT Neutrino Telescope, *JINST* 13 (2018) P05035. doi:10.1088/1748-0221/13/05/P05035.

- [21] P. Barrow, et al., Qualification Tests of the R11410-21 Photomultiplier Tubes for the XENON1T Detector, JINST 12 (2017) P01024. doi:10.1088/1748-0221/12/01/P01024. arXiv:1609.01654.
- [22] V. C. Antochi, et al., Improved quality tests of R11410-21 photomultiplier tubes for the XENONnT experiment, JINST 16 (2021) P08033. doi:10.1088/1748-0221/16/08/P08033. arXiv:2104.15051.
- [23] D. van Eijk, J. Schneider, M. Unland, Characterisation of Two PMT Models for the IceCube Upgrade mDOM, PoS ICRC2019 (2019) 1022. doi:10.22323/1.358.1022.
- [24] CAEN S.p.A., V1751: 4/8 Channel 10 bit 2/1 GS/s Digitizer, available at <https://www.caen.it/products/v1751/> (accessed on December 31, 2022), 2022.
- [25] H. Q. Zhang, et al., Comparison on PMT Waveform Reconstructions with JUNO Prototype, JINST 14 (2019) T08002. doi:10.1088/1748-0221/14/08/T08002. arXiv:1905.03648.
- [26] W-IE-NE-R, MPOD High Voltage module, available at <https://www.wiener-d.com/product/mpod-hv-module/> (accessed on December 31, 2022), 2022.
- [27] NKT Photonics, PILAS: picosecond pulsed diode lasers, available at <https://www.nktphotonics.com/products/pulsed-diode-lasers/pilas/> (accessed on December 31, 2022), 2022.
- [28] CAEN S.p.A., CAENDigitizer Library: Library of functions for CAEN Digitizers high level management, available at <https://www.caen.it/products/caendigitizer-library/> (accessed on December 31, 2022), 2022.
- [29] Net-SNMP Team, Net-SNMP, available at <https://net-snmp.sourceforge.io/> (accessed on December 31, 2022), 2019.
- [30] PyVISA Authors, PyVISA: Control your instruments with Python, available at <https://pyvisa.readthedocs.io/en/latest/> (accessed on December 31, 2022), 2022.
- [31] Beijing Hamamatsu Photon Techniques INC., CR365-01, available at <http://www.bhphoton.com/site/zh/product/guangdianqijian/duanchuangxingguangdianbeizengguan/1502326956990599170.html> (accessed on December 31, 2022), 2022.
- [32] T. Kaptanoglu, Characterization of the Hamamatsu 8" R5912-MOD Photomultiplier Tube, Nucl. Instrum. Meth. A 889 (2018) 69–77. doi:10.1016/j.nima.2018.01.086. arXiv:1710.03334.
- [33] H. Q. Zhang, et al., Study on relative collection efficiency of PMTs with spotlight, Radiat Detect Technol Methods 3 (2019). doi:10.1007/s41605-019-0099-x.
- [34] R. Brun, F. Rademakers, ROOT — An object oriented data analysis framework, Nuclear Instruments and Methods in Physics Research Section A: Accelerators, Spectrometers, Detectors and Associated Equipment 389 (1997) 81–86. URL: <https://www.sciencedirect.com/science/article/pii/S016890029700048X>. doi:10.1016/S0168-9002(97)00048-X.
- [35] H. Q. Zhang, et al., Gain and charge response of 20" MCP and dynode PMTs, JINST 16 (2021) T08009. doi:10.1088/1748-0221/16/08/T08009. arXiv:2103.14822.
- [36] G. Cowan, Statistical data analysis, in: Statistical data analysis, 1998.
- [37] W. Luo, Q. Liu, Y. Zheng, Z. Wang, S. Chen, Reconstruction algorithm for a novel Cherenkov scintillation detector, JINST 18 (2023) P02004. doi:10.1088/1748-0221/18/02/P02004. arXiv:2209.13772.
- [38] Z. Chen, et al., Analysis of secondary electron yield and energy spectrum of metal materials based

- on Furman model, IEEE, 2020, pp. 152–155. doi:10.1109/ICSM50554.2020.9261703.
- [39] S. Shin, et al., Advances in the Large Area Picosecond Photo-Detector (LAPPD): 8" x 8" MCP-PMT with Capacitively Coupled Readout (2022). arXiv:2212.03208.
- [40] W. Cao, et al., Secondary electron emission characteristics of the Al₂O₃/MgO double-layer structure prepared by atomic layer deposition, *Ceramics International* 47 (2021) 9866–9872. URL: <https://www.sciencedirect.com/science/article/pii/S0272884220337299>. doi:<https://doi.org/10.1016/j.ceramint.2020.12.128>.
- [41] P. B. Coates, The origins of afterpulses in photomultipliers, *Journal of Physics D: Applied Physics* 6 (1973) 1159–1166. URL: <https://doi.org/10.1088/0022-3727/6/10/301>. doi:10.1088/0022-3727/6/10/301.
- [42] K. J. Ma, et al., Time and Amplitude of Afterpulse Measured with a Large Size Photomultiplier Tube, *Nucl. Instrum. Meth. A* 629 (2011) 93–100. doi:10.1016/j.nima.2010.11.095. arXiv:0911.5336.
- [43] K. Abe, et al. (XMASS), Development of low-background photomultiplier tubes for liquid xenon detectors, *JINST* 15 (2020) P09027. doi:10.1088/1748-0221/15/09/P09027. arXiv:2006.00922.
- [44] R. Zhao, et al., Afterpulse measurement of JUNO 20-inch PMTs (2022). arXiv:2207.04995.
- [45] J. W. Hardin, J. M. Hilbe, *Generalized Linear Models and Extension*, Stata Press, 2018.
- [46] M. Teich, K. Matsuo, B. Saleh, Excess Noise Factors for Conventional and Superlattice Avalanche Photodiodes and Photomultiplier Tubes, *IEEE Journal of Quantum Electronics* 22 (1986) 1184–1193. doi:10.1109/JQE.1986.1073137.
- [47] D. Barnhill, F. Suarez, K. Arisaka, B. Garcia, J. P. Gongora, A. Lucero, I. Navarro, T. Ohnuki, A. Risi, A. Tripathi, Testing of photomultiplier tubes for use in the surface detector of the Pierre Auger Observatory, *Nucl. Instrum. Meth. A* 591 (2008) 453–466. doi:10.1016/j.nima.2008.01.088.